Uniquely anisotropic mechanical and thermal responses of hybrid organic-inorganic perovskites under uniaxial strain

Muhammad Akif Rahman[1] and Ashutosh Giri[1]

Department of Mechanical, Industrial, and Systems Engineering,
University of Rhode Island

(*Electronic mail: ashgiri@uri.edu)

(Dated: September 8, 2021)

The complete understanding of the mechanical and thermal responses to strain in hybrid organic-inorganic perovskites holds great potential for their proper functionalities in a range of applications such as in photovoltaics, thermoelectrics and flexible electronics. In this work, we conduct systematic atomistic simulations on methyl ammonium lead iodide, which is the prototypical hybrid inorganic-organic perovskite, to investigate the changes in their mechanical and thermal transport responses under uniaxial strain. We find that the mechanical response and the deformation mechanisms are highly dependent on the direction of the applied uniaxial strain with a characteristic ductile- or brittle-like failure accompanying unaxial tension. Moreover, while most materials shrink in the two lateral directions when stretched, we find that the ductile behavior in hybrid perovskites can lead to a very unique mechanical response where negligible strain occurs along one lateral direction while length contraction occurs in the other direction due to uniaxial tension. This anisotropy in the mechanical response is also shown to manifest in an anisotropic thermal response of the hybrid perovskite where the anisotropy in thermal conductivity increases by up to 30% in comparison to the unstrained case before plastic deformation occurs at higher strain levels. Along with the anisotropic responses of these physical properties, we find that, uniaxial tension leads to ultralow thermal conductivities that are well below the value predicted with a minimum thermal conductivity model, which highlights the potential of strain engineering to tune the physical properties of hybrid organic-inorganic perovskites.

I. INTRODUCTION

Hybrid organic-inorganic perovskites are endowed with remarkable physical properties, which derive from their unique chemical and structural makeup.[1,2] Since their first successful demonstration as materials for photovoltaic applications little more than a decade ago,[3] these materials have demonstrated exceptional optical, electrical and thermal properties, placing them as one of the premier materials for emerging technologies such as in thermoelectrics, electrochemical energy storage, and solar cells.[4–11] More recently, these materials have been integrated as thin film absorbers on flexible polymer substrates and in shape recoverable device architectures for flexible electronics.[12,13] As such, a comprehensive understanding of their mechanical and thermal properties that inherently set the limitations of hybrid organic-inorganic perovskites as materials for deformable electronics is quintessential for their realization and further improvement in efficiencies in such applications.

Recent studies have focused on understanding heat transfer and lattice dynamics of hybrid perovskites from both experimental and computational perspectives.[14–26] Experimental measurements report thermal conductivities in the range of 0.34 to 0.73 $\mathrm{W\,m^{-1}\,K^{-1}}$ for various three-dimensional single crystal hybrid perovskites. The variation in the ultralow thermal conductivities between the different hybrid perovskites has been attributed to changes in the speed of sound, which are mainly dictated by the elastic properties of the inorganic framework.[19] The ultralow room temperature thermal conductivity of these materials and the hot phonon bottleneck have been prescribed to low group velocities and strong anharmonic phonon-phonon scattering that are prevalent in these types of structures mainly due to their low elastic stiffnesses.[17,18,25,27] Therefore, these findings suggest that the thermal properties of hybrid perovskites are strongly associated with their mechanical and structural properties.

In terms of the mechanical properties, nanoindentation studies and laser-based experiments have highlighted the unique anisotropy in elastic properties of hybrid perovskites with the measured Young's modulus in the range of 7 to 20 GPa.[12,28–30] Computational studies conducted with first principles calculations have corroborated the anisotropy in Young's modulus and have also demonstrated that the low shear modulus in hybrid organic-inorganic perovskites can be beneficial for applications in compliant devices where large deformations are demanded.[31] Furthermore, polycrystalline $CH_3NH_3PbI_3$ ($MAPbI_3$) have been shown to possess nanoductility surpassing their single crystal counterparts, which was attributed to the extensive and continuous amorphization in the polycrystalline structure.[32]

Another unique mechanical property predicted by computational studies for hybrid perovskites (and other oxide based perovskites) is the possibility of negative Poisson's ratio in certain directions.[31,33,34] Based on the elastic constant tensor calculated from first-principle calculations, Ji *et al.*[34] have shown that the orthorhombic phase of $\mathrm{MAPbI_3}$ and other similar hybrid perovskites can demonstrate a negative Poisson's ratio in certain directions due to the rotational motion of the $\mathrm{PbI_6}$ octahedron.[34] In most materials, a uniaxial tension in the orthogonal direction leads to the shrinking of the lateral directions; these materials are characterized by a positive Poisson's ratio. However, there are a certain class of materials, although rare, that have a negative Poisson's ratio (a.k.a. auxetic materials)[35–41] and are characterized with an expansion in the lateral directions when stretched in the orthogonal direction such as that predicted by Ji *et al.*[34] for hybrid perovskites in certain directions. These materials are often accompanied by enhanced physical properties that are beneficial for different kinds of applications.[42–47] For example, auxetic materials are used in applications ranging from medicine and tissue engineering, flexible photovoltaics and in aerospace and defense.[48–51] Auxetic behavior has been shown for honeycomb structures and open cell foams,[44,52] cubic metals strained along non axial directions,[46,53] two-dimensional materials,[54–56] select types of polymers,[37–39,57,58] and metal organic frameworks.[59,60] However, direct observation of auxeticity in hybrid organic-inorganic perovskites has not yet been demonstrated and only inferences based on the elastic tensor predicted from first-principle calculations have been made.[34] Therefore, a systematic investigation from an atomistic perspective of the mechanical as well as thermal responses of hybrid organic-inorganic perovskites under uniaxial strain would shed light on the microscopic mechanisms dictating these physical properties and would also be beneficial for a range of applications that are reliant on these novel materials.

Through atomistic simulations, in this work, we show that the mechanical response and the deformation mechanism in hybrid perovskites are highly dependent on the direction of the applied uniaxial strain with a characteristic ductile deformation under uniaxial tension along [100] or [010] directions, whereas brittle failure occurs when the tensile loading is applied along the [001] direction. With uniaxial tension along the [100] or [010] orthogonal direction, an anisotropic mechanical response is observed in the two lateral directions with a length contraction in the [001] direction while a negligible change in the length occurs along the other direction. We also find an anisotropic thermal response to unaxial strain, where the thermal conductivity along the length contraction direction remains unchanged, whereas the thermal conductivity in the plane of the uniaxial tensile loading [001] decreases monotonically, thus increasing the anisotropy in thermal conductivity by up to 30 % before plastic deformation occurs.

II. METHODOLOGY

We study the prototypical hybrid organic-inorganic perovskite, MAPbI$_3$, via molecular dynamics (MD) simulations. The interatomic potential utilized in our MD simulations is the *ab initio*-based potential (MYP forcefield) developed by Mattoni *et al.*[61] This potential has been shown to predict the correct vibrational physics (including thermal properties of MAPbI$_3$)[18,23] and also shown to correctly predict their elastic properties.[32] Moreover, the potential was developed specifically to replicate the energy profile as the molecular constituents reorient themselves with respect to the deforming inorganic framework, which further validates the use of this potential for investigation of mechanical response to strain of these materials. We use the LAMMPS package for all of our simulations.[62]

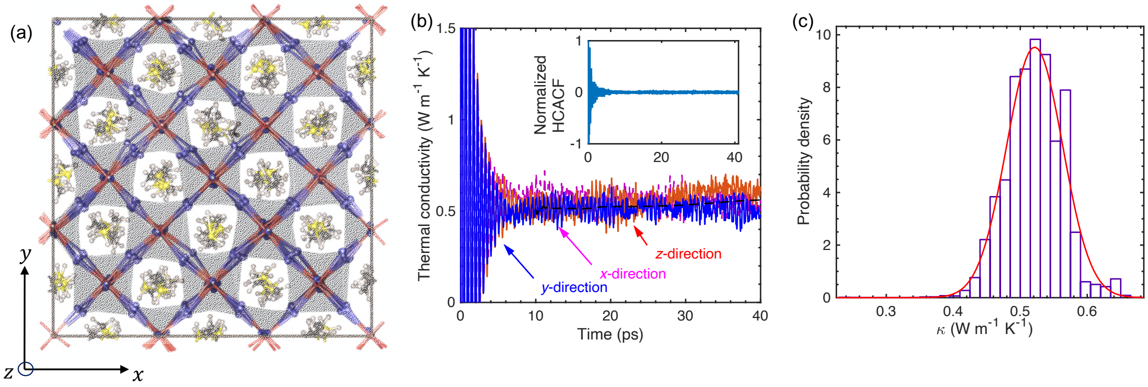

Figure 1. (a) Schematic cross-section of the equilibrated computational domain for tetragonal CH$_3$NH$_3$PbI$_3$ at room temperature. (b) Green-Kubo predicted thermal conductivity of MAPbI$_3$ as a function of the integration time at 300 K. (inset) HCACF vs. time for MAPbI$_3$. (c) An error of ∼8-11 % is calculated based on predictions from 10 independent simulations (κ=0.52±0.04 W m-1 K-1).

Using the MYP potential,[61] the initial computational domain for MAPbI$_3$ is equilibrated for a total of 1 ns at 0 bar pressure with a time step of 1 fs under the Nose-Hoover thermostat (at room temperature) and barostat;[63] this is the NPT integration where the number of particles, pressure and temperature are held constant during the simulation. Following the NPT integration, an additional equilibration under the NVT integration (where the volume and number of particles is held constant during the simulation) is performed. Note, during equilibration and the subsequent simulation to investigate the thermal and mechanical properties, periodic boundary conditions are applied in all directions and a time step of 1 fs is utilized. The size of the computational domain is 26.45 × 26.55 × 112.90 Å^3. The cross-section of the equilibrated computational domain for $MAPbI_3$ is shown in Fig. 1a. The x-, y-, and z-directions as shown in Fig. 1a reflect the [100], [010], and [001] directions, respectively.

To assess the mechanical properties, a uniaxial deformation in the three principle (x-, y- and z-) directions is applied at a strain rate of 10^8 s^{-1}. During the uniaxial loading, the other periodic boundaries are held under "stress-free" conditions (at 0 bars) with the NPT integration. To generate the stress-strain relationships for our $MAPbI_3$, the stress and strain along the three principle directions are calculated every 0.1 ps.

To understand how the structural and mechanical anisotropy affects the thermal properties of $MAPbI_3$, the thermal conductivities along the three principle directions at different strain conditions are predicted via the Green-Kubo (GK) approach under the equilibrium molecular dynamics (EMD) framework. The thermal conductivity within this framework is calculated as,

$$\kappa_{x,y,z} = \frac{1}{k_B V T^2} \int_0^\infty \langle J_{x,y,z}(t) J_{x,y,z}(0) \rangle dt, \tag{1}$$

where, t is time, T and V are the temperature and volume of the systems, respectively, and $\langle J_{x,y,z}(t) J_{x,y,z}(0) \rangle$ is the component of the heat current autocorrelation function (HCACF) in the prescribed three-principle directions and is given as,

$$\mathbf{J} = \frac{1}{V} \left(\sum_i \mathbf{v}_i \varepsilon_i + \sum_i \mathbf{S}_i \cdot \mathbf{v}_i \right), \tag{2}$$

where, $\mathbf{v}_i$, ε_i and $\mathbf{S}_i$ are the velocity, energy and stress of atom i respectively.[64] The total correlation time period for the integration of the HCACF is set to 40 ps. This ensures that the HCACF decays to zero as shown in the inset Fig. 1b. The heat current is computed every 10 time steps followed by integration of the HCACF to calculate the converged thermal conductivity for the $MAPbI_3$ domain. The converged thermal conductivity is determined from the integration from 10 ps to 40 ps as shown in Fig. 1b (dashed line). Utilizing this procedure, we conduct 10 independent simulations with different initial conditions to determine the uncertainty of ∼8-11 % as exemplified in Fig. 1c showing the distribution of thermal conductivities of our unstrained $MAPbI_3$ (with κ=0.52±0.04 W m^{-1} K^{-1}).

[redacted]

[redacted]

III. RESULTS AND DISCUSSION

Figures 3a and 3b, show the representative stress-strain curves from the uniaxial tensile loading along the *y*- and *z*- directions, respectively. Note, the stress-strain relationship in the *x*- and *y*-directions are similar, therefore only the results for the uniaxial loading along the *y*-direction is shown. The slopes of the linear regions in the stress-strain curves, as shown by the dashed-lines, are used to predict the Young's modulus. In agreement with previous results from nanoindentation measurements and first principles calculations,[28,34,68] the Young's modulus for $MAPbI_3$ under uniaxial tensile loading along the *y*- and *z*-directions are 13.6 GPa and 8.4 GPa, respectively. It is interesting to note that although plastic deformation initiates at similar strain levels in the two directions, the ultimate tensile strength in the *y*-direction is higher as compared to that along the *z*-direction. This anisotropy in the mechanical response can be largely attributed to the anisotropic

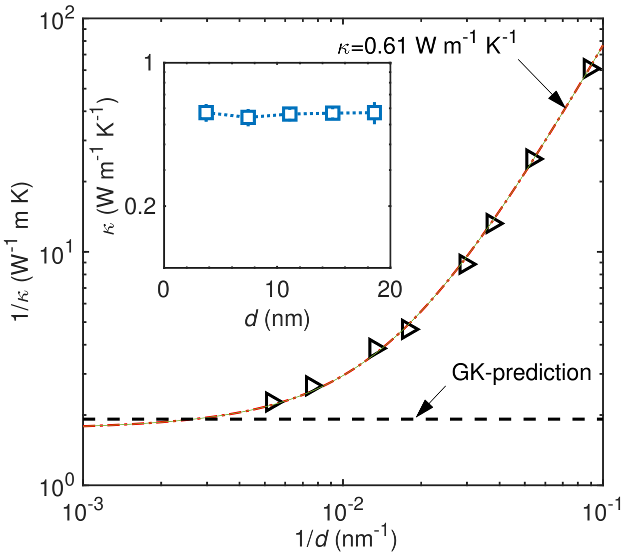

[redacted]

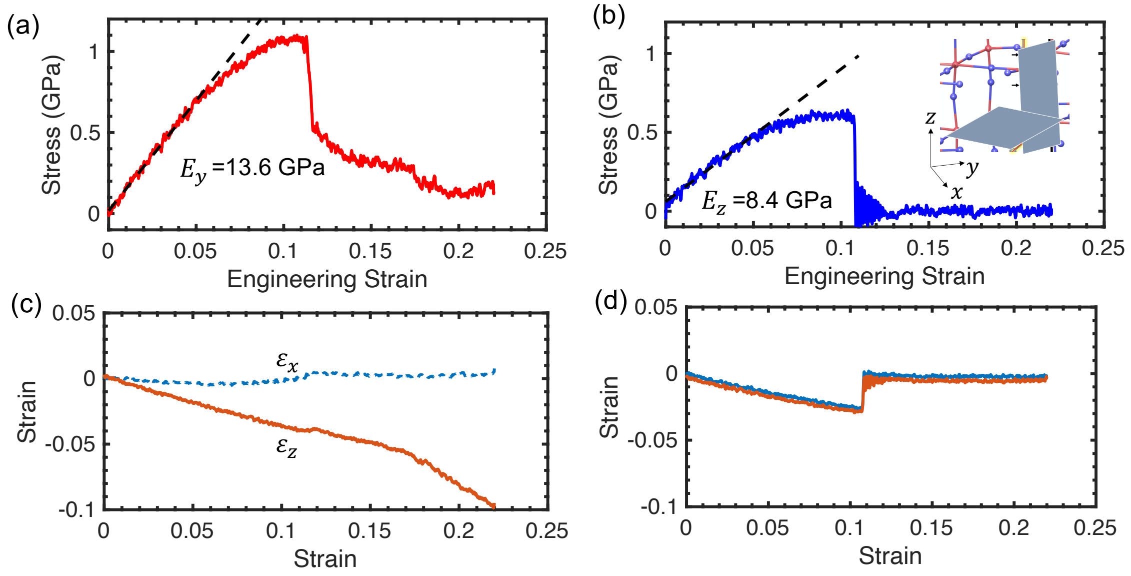

Figure 3. Characteristic stress-strain curves under uniaxial tensile loading along (a) y- and (b) z-directions. Note, stress-strain curves for uniaxial loading along x- and y-directions are similar, therefore we only show the results for uniaxial tension along the y-direction. The slope of the linear elastic region as represented by the dashed-line corresponds to the Young's modulus. The resultant strain in the two orthogonal directions versus the applied strain in the (c) y- and (d) z- directions.

structure of the inorganic framework, where the lead atoms are bonded to 4 iodide atoms in the *xy*-plane, whereas the lead atoms are bonded to only 2 iodide atoms within the plane parallel to the *z*-axis as illustrated in the inset of Fig 3b. The relative changes in the bond environments along the two orthogonal planes lead to a more compliant mechanical response under uniaxial tension in the *z*-direction in comparison to that in either the *x*- or the *y*-directions.

More interestingly, the uniaxial tensile loading simulations reveal another unique anisotropic mechanical behavior of $MAPbI_3$ where the length of the computational domain in the *x*-direction remains constant while the length in the *z*-direction is decreased during uniaxial tensile loading in the *y*-direction. This is quantitatively shown in Fig. 3c where we plot the strain in the two lateral directions as a function of the applied strain in the *y*-direction. In contrast, when tension is applied in the *z*-direction, the computational domain shrinks in both the *x*- and *y*-directions in response to the applied strain as shown in Fig. 3c.

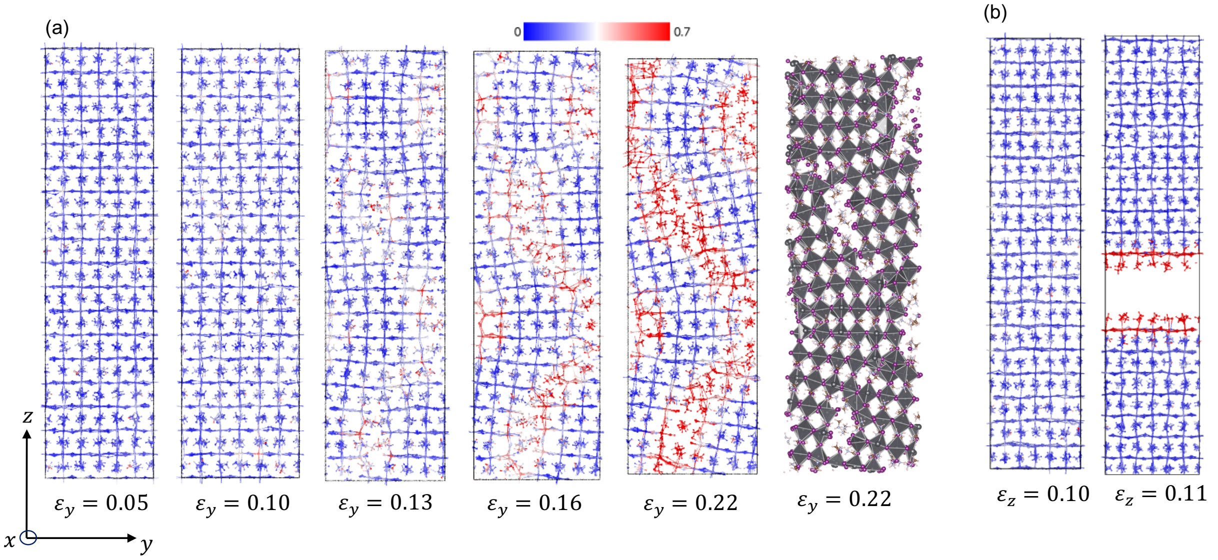

Figure 4. Snapshots of the corss-sections of $CH_3NH_3PbI_3$ computational domain showing calculations of atomic level strain relative to the relaxed computational domain at (a) various ε_y and (b) ε_z. Ductile failure dominates beyond the elastic region when the applied uniaxial tensile strain is along either *x*- or *y*-direction. The ductile deformation orginates from the distortion of the PbI_6 octahedron. However, brittle failure occurs when uniaxial strain is applied along the *z*-direction.

From the stress-strain curves shown in Figs. 3a and 3b, it can be inferred that the mechanism of deformation under uniaxial tensile loading in the two orthogonal directions are also different. While ductile failure occurs during uniaxial tension along the *x*- or *y*-directions, a more brittle-like failure is observed at $\sim$10 % strain level during uniaxial loading along the *z*-direction. This is schematically shown in Figs. 4a and 4b, which shows the computational domains under uniaxial deformation when strain is applied in the y- and z-directions, respectively. To highlight the local deformation mechanisms, the atoms are colored in terms of the associated von Mises strain as calculated in Ref. 69. Figure 4a shows the local strain under uniaxial tension along the y-direction at different strain levels. At 5 % strain level, no observable stress localization occurs. However, as the strain is increased beyond 10 %, stress localization (as represented by the red colored atoms) spreads throughout the structure, which ultimately leads to a ductile failure. As shown by the corresponding figure highlighting the octahedral tilts for ε_y=0.22 in Fig. 4a, the ductile behavior in $MAPbI_3$ can be ascribed to the rotation and tilting of the octahedral cages due to the applied strain. This deformation mechanism makes the crystal more compliant and leads to the unique strain response as shown in Fig. 3a and Fig. 3c; although our results do not directly support the hypothesized auxetic behaviour in $MAPbI_3$,[34] the unique mechanical response where lateral contraction occurs in one direction, while the length in the other lateral direction does not change separates these materials from other crystalline solids where it is usually observed that length contractions along both lateral directions occur due to uniaxial tensile force. [redacted] In contrast, when uniaxial strain is applied in the z-direction, stress localization occurs along a specific plane of atoms parallel to the xy-plane leading to a more brittle-like failure as shown in Fig. 4b. [redacted]

Next, to understand how the structural and mechanical anisotropy affect the thermal properties of $MAPbI_3$, the thermal conductivity is calculated with the GK formalism. For the equilibrated computational domain without the application of uniaxial strain, the thermal conductivity along all three principle directions are similar within the 8-11 % uncertainties that are associated with our GK predictions ($\kappa \sim 0.52 \pm 0.04$ W m^{-1} K^{-1}as shown in Fig. 5a) and agree well with experi-

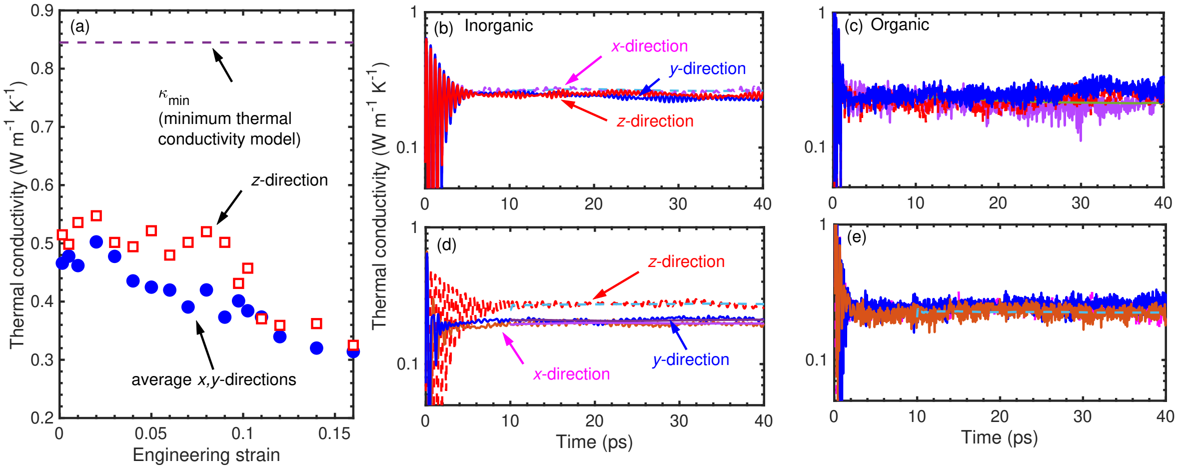

Figure 5. (a) Thermal conductivity of $MAPbI_3$ along the xy-plane and z-direction as a function of applied uniaxial strain along the y-direction, ε_y. For comparison, the dashed line shows predictions from the minimum thermal conductivity model. Separate contributions from the (b) inorganic and (c) organic constituents to the total thermal conductivity at ε_y=0. Separate contributions from the (d) inorganic and (e) organic constituents to the total thermal conductivity at ε_y=0.08.

mentally measured room temperature thermal conductivity for $MAPbI_3$.[15,19] However, as shown in Fig. 5a, the application of tensile strain along the x-direction leads to a monotonic reduction in thermal conductivity in both the x- and y-directions (solid circles), whereas the change in the thermal conductivity in the z-direction is negligible (in the elastic region of the stress-strain relationship, which is up to ∼8 % strain; hollow squares). Beyond the strain where the ultimate strength of the material is reached, thermal conductivity decreases for all three directions as shown in Fig. 5a.

[redacted] This model is usually applied (and often correctly predicts the thermal conductivity) for pure amorphous solids where non-propagating vibrations (namely diffusons and locons) are the dominant heat carriers.[71] The main assumptions in calculating κ_{min} for a disordered solid are that the "mean-free-paths" of vibrations in the solid are limited to the spacings between adjacent atoms and the lifetimes of these heat-carrying oscillations are one half the period of vibration (see Refs. 24 and 70 for details). The GK-predicted thermal conductivities for all strain levels as shown in Fig. 5a are well below the prediction from this minimum limit model suggesting that the explanation of energy propagation through thermal interactions on the order of the vibrational wavelength cannot explain the heat conduction mechanism in $MAPbI_3$ for both the unstrained and strained cases. Instead, the ultralow thermal conductivity for unstrained $MAPbI_3$ has been attributed to strong acoustic-optical phonon scattering that result from the significant overlap in energy of the acoustic and optical phonons.[18,72] The application of strain further enhances these scattering mechanisms and leads to an overall decrease in thermal conductivity.

To better understand the effect of uniaxial strain on the anisotropic thermal response in $MAPbI_3$, we separate the contributions from the inorganic and organic constituents (as shown in Figs. 5b-e) by analyzing the total heat flux. Using Eq. 2, the thermal conductivity contributions from the inorganic and organic constituents can be easily separated by calculating the heat flux for the atoms of the methylammonium cations separately from the atoms forming the inorganic framework (Pb and I atoms). This is shown in Figs. 5b and 5c for the inorganic and organic, respectively at 0 % strain level. The contributions to the total heat conduction from the inorganic and organic constituents are similar as shown in Figs. 5b and 5c for the respective. However, at 8 % strain, the anisotropy in thermal conductivity originates from the inorganic framework leading to an increased contribution to the total thermal conductivity from the inorganic framework along the z-direction, whereas the contributions from the organic constituents are unaffected by the strain (see Fig. 5e).

The change in thermal conductivity upon mechanical loading (up to the elastic region) can be used in applications such as thermal switches and diodes.[73] Usually when tensile force is applied to a crystalline solid, the thermal conductivity decreases due to phonon softening.[74,75] Upon compression, phonon hardening generally leads to enhanced thermal conductivity. The uniaxial tension along the x- or y-directions in $MAPbI_3$ leads to compression in the z-direction (see Fig. 3c). However, the thermal conductivity in the z-direction remains unchanged in the linear elastic region, which is likely due to the competing effects of phonon hardening that increases thermal conductivity and phonon scattering that leads to a reduction in thermal conductivity. These competing mechanisms can lead to as much as 30 % increase in thermal conductivity anisotropy in $MAPbI_3$ as the thermal conductivity monotonically decreases in the x- and y-directions due to uniaxial tension along one of these directions (see Fig. 5a). Taken together with the mechanically compliant nature of hybrid perovskites along certain directions, enhancement in thermal conductivity anisotropy due to strain engineering in these novel materials could be beneficial for applications such as in flexible electronics where preferential energy transfer along selected directions is required.[76]

IV. CONCLUSION

In summary, the mechanical and thermal responses under uniaxial strain of the prototypical hybrid organic-inorganic perovskite, $MAPbI_3$, are investigated via molecular dynamics simulations. It is found that the mechanical response and the deformation mechanism is highly dependent on the direction of the uniaxial strain with a characteristic ductile deformation under uniaxial strain along [100] or [010] directions, whereas brittle failure occurs when the tensile loading is applied along the [001] direction. Furthermore, when uniaxial tension is applied along the [100] or [010] directions, an anisotropic mechanical response is observed in the two lateral directions with a length decrease in the [001] direction and a negligible change in the length along the other lateral direction. The anisotropy in the mechanical response also manifests in an anisotropic thermal response where the thermal conductivity along the length contraction direction remains unchanged during the elastic response under uniaxial tensile strain, whereas the thermal conductivity in the plane of the uniaxial tensile loading [001] decreases monotonically, thus increasing the anisotropy in thermal conductivity by up to 30 %. The combination of these anisotropic physical properties positions hybrid organic-inorganic perovskites as an emerging class of multifunctional materials with potential applications in the development of sensors for pressure detection and shock absorbing materials such as in 'smart' body armors.[77,78]

ACKNOWLEDGMENTS

This manuscript is based upon work supported by the Office of Naval Research, Grant No. N00014-21-1-2622. The work is also partially supported by the National Science Foundation (NSF Award No. 2119365).

AUTHOR DECLARATIONS

Conflict of interest

The authors have no conflicts to disclose.

DATA AVAILABILITY STATEMENT

AVAILABILITY OF DATA	**STATEMENT OF DATA AVAILABILITY**
Data available on request from the authors	The data that support the findings of this study are available from the corresponding author upon reasonable request.

REFERENCES

[1] J. Huang, Y. Yuan, Y. Shao, and Y. Yan, "Understanding the physical properties of hybrid perovskites for photovoltaic applications," Nature Reviews Materials **2**, 1–19 (2017).

[2] G. Grancini and M. K. Nazeeruddin, "Dimensional tailoring of hybrid perovskites for photovoltaics," Nature Reviews Materials **4**, 4–22 (2019).

[3] A. Kojima, K. Teshima, Y. Shirai, and T. Miyasaka, "Organometal halide perovskites as visible-light sensitizers for photovoltaic cells," Journal of the American Chemical Society **131**, 6050–6051 (2009).

[4] L. Dou, A. B. Wong, Y. Yu, M. Lai, N. Kornienko, S. W. Eaton, A. Fu, C. G. Bischak, J. Ma, T. Ding, *et al.*, "Atomically thin two-dimensional organic-inorganic hybrid perovskites," Science **349**, 1518–1521 (2015).

[5] M. Saliba, T. Matsui, J.-Y. Seo, K. Domanski, J.-P. Correa-Baena, M. K. Nazeeruddin, S. M. Zakeeruddin, W. Tress, A. Abate, A. Hagfeldt, *et al.*, "Cesium-containing triple cation perovskite solar cells: improved stability, reproducibility and high efficiency," Energy & environmental science **9**, 1989–1997 (2016).

[6] J. Burschka, N. Pellet, S.-J. Moon, R. Humphry-Baker, P. Gao, M. K. Nazeeruddin, and M. Grätzel, "Sequential deposition as a route to high-performance perovskite-sensitized solar cells," Nature **499**, 316–319 (2013).

[7] H. Zhu, Y. Fu, F. Meng, X. Wu, Z. Gong, Q. Ding, M. V. Gustafsson, M. T. Trinh, S. Jin, and X. Y. Zhu, "Lead halide perovskite nanowire lasers with low lasing thresholds and high quality factors," Nature materials **14**, 636–642 (2015).

[8] H. J. Snaith, "Perovskites: the emergence of a new era for low-cost, high-efficiency solar cells," The journal of physical chemistry letters **4**, 3623–3630 (2013).

[9] Y. Fang, Q. Dong, Y. Shao, Y. Yuan, and J. Huang, "Highly narrowband perovskite single-crystal photodetectors enabled by surface-charge recombination," Nature Photonics **9**, 679–686

(2015).

[10]M. Yuan, L. N. Quan, R. Comin, G. Walters, R. Sabatini, O. Voznyy, S. Hoogland, Y. Zhao, E. M. Beauregard, P. Kanjanaboos, *et al.*, "Perovskite energy funnels for efficient light-emitting diodes," Nature nanotechnology **11**, 872–877 (2016).

[11]B. Saparov and D. B. Mitzi, "Organic–inorganic perovskites: structural versatility for functional materials design," Chemical reviews **116**, 4558–4596 (2016).

[12]M. Park, H. J. Kim, I. Jeong, J. Lee, H. Lee, H. J. Son, D.-E. Kim, and M. J. Ko, "Mechanically recoverable and highly efficient perovskite solar cells: investigation of intrinsic flexibility of organic–inorganic perovskite," Advanced Energy Materials **5**, 1501406 (2015).

[13]P. Docampo, J. M. Ball, M. Darwich, G. E. Eperon, and H. J. Snaith, "Efficient organometal trihalide perovskite planar-heterojunction solar cells on flexible polymer substrates," Nature communications **4**, 1–6 (2013).

[14]M. A. Haque, S. Kee, D. R. Villalva, W.-L. Ong, and D. Baran, "Halide perovskites: thermal transport and prospects for thermoelectricity," Advanced Science **7**, 1903389 (2020).

[15]A. Pisoni, J. Jacimovic, O. S. Barisic, M. Spina, R. Gaál, L. Forró, and E. Horváth, "Ultralow thermal conductivity in organic–inorganic hybrid perovskite $CH_3NH_3PbI_3$," The journal of physical chemistry letters **5**, 2488–2492 (2014).

[16]T. Hata, G. Giorgi, and K. Yamashita, "The effects of the organic–inorganic interactions on the thermal transport properties of $CH_3NH_3PbI_3$," Nano letters **16**, 2749–2753 (2016).

[17]X. Qian, X. Gu, and R. Yang, "Lattice thermal conductivity of organic-inorganic hybrid perovskite $CH_3NH_3PbI_3$," Applied Physics Letters **108**, 063902 (2016).

[18]M. Wang and S. Lin, "Anisotropic and ultralow phonon thermal transport in organic–inorganic hybrid perovskites: atomistic insights into solar cell thermal management and thermoelectric energy conversion efficiency," Advanced Functional Materials **26**, 5297–5306 (2016).

[19]G. A. Elbaz, W.-L. Ong, E. A. Doud, P. Kim, D. W. Paley, X. Roy, and J. A. Malen, "Phonon speed, not scattering, differentiates thermal transport in lead halide perovskites," Nano letters **17**, 5734–5739 (2017).

[20]T. Liu, S.-Y. Yue, S. Ratnasingham, T. Degousée, P. Varsini, J. Briscoe, M. A. McLachlan, M. Hu, and O. Fenwick, "Unusual thermal boundary resistance in halide perovskites: A way to tune ultralow thermal conductivity for thermoelectrics," ACS applied materials & interfaces **11**, 47507–47515 (2019).

[21]R. Heiderhoff, T. Haeger, N. Pourdavoud, T. Hu, M. Al-Khafaji, A. Mayer, Y. Chen, H.-C.

Scheer, and T. Riedl, “Thermal conductivity of methylammonium lead halide perovskite single crystals and thin films: A comparative study,” The Journal of Physical Chemistry C **121**, 28306–28311 (2017).

[22] Y. Wang, R. Lin, P. Zhu, Q. Zheng, Q. Wang, D. Li, and J. Zhu, “Cation dynamics governed thermal properties of lead halide perovskite nanowires,” Nano letters **18**, 2772–2779 (2018).

[23] C. Caddeo, C. Melis, M. I. Saba, A. Filippetti, L. Colombo, and A. Mattoni, “Tuning the thermal conductivity of methylammonium lead halide by the molecular substructure,” Physical Chemistry Chemical Physics **18**, 24318–24324 (2016).

[24] A. Giri, A. Z. Chen, A. Mattoni, K. Aryana, D. Zhang, X. Hu, S.-H. Lee, J. J. Choi, and P. E. Hopkins, “Ultralow thermal conductivity of two-dimensional metal halide perovskites,” Nano letters **20**, 3331–3337 (2020).

[25] H. Ma, C. Li, Y. Ma, H. Wang, Z. W. Rouse, Z. Zhang, C. Slebodnick, A. Alatas, S. P. Baker, J. J. Urban, *et al.*, “Supercompliant and Soft $(CH_3NH_3)_3Bi_2I_9$ Crystal with Ultralow Thermal Conductivity,” Physical review letters **123**, 155901 (2019).

[26] T. Zhu and E. Ertekin, “Mixed phononic and non-phononic transport in hybrid lead halide perovskites: glass-crystal duality, dynamical disorder, and anharmonicity,” Energy & Environmental Science **12**, 216–229 (2019).

[27] A. C. Ferreira, A. Létoublon, S. Paofai, S. Raymond, C. Ecolivet, B. Rufflé, S. Cordier, C. Katan, M. I. Saidaminov, A. A. Zhumekenov, *et al.*, “Elastic softness of hybrid lead halide perovskites,” Physical Review Letters **121**, 085502 (2018).

[28] S. Sun, Y. Fang, G. Kieslich, T. J. White, and A. K. Cheetham, “Mechanical properties of organic–inorganic halide perovskites, $CH_3NH_3PbX_3$ (X= I, Br and Cl), by nanoindentation,” Journal of Materials Chemistry A **3**, 18450–18455 (2015).

[29] P.-A. Mante, C. C. Stoumpos, M. G. Kanatzidis, and A. Yartsev, “Directional negative thermal expansion and large poisson ratio in $CH_3NH_3PbI_3$ perovskite revealed by strong coherent shear phonon generation,” The journal of physical chemistry letters **9**, 3161–3166 (2018).

[30] A. Létoublon, S. Paofai, B. Ruffle, P. Bourges, B. Hehlen, T. Michel, C. Ecolivet, O. Durand, S. Cordier, C. Katan, *et al.*, “Elastic constants, optical phonons, and molecular relaxations in the high temperature plastic phase of the $CH_3NH_3PbBr_3$ hybrid perovskite,” The journal of physical chemistry letters **7**, 3776–3784 (2016).

[31] T. Feng and X. Ruan, “Prediction of spectral phonon mean free path and thermal conductivity with applications to thermoelectrics and thermal management: a review,” Journal of Nanomate-

rials **2014** (2014).

[32] J. Yu, M. Wang, and S. Lin, "Probing the soft and nanoductile mechanical nature of single and polycrystalline organic–inorganic hybrid perovskites for flexible functional devices," Acs Nano **10**, 11044–11057 (2016).

[33] L. Dong, D. S. Stone, and R. S. Lakes, "Softening of bulk modulus and negative Poisson ratio in barium titanate ceramic near the Curie point," Philosophical magazine letters **90**, 23–33 (2010).

[34] L.-J. Ji, S.-J. Sun, Y. Qin, K. Li, and W. Li, "Mechanical properties of hybrid organic-inorganic perovskites," Coordination Chemistry Reviews **391**, 15–29 (2019).

[35] E. Kittinger, J. Tichỳ, and E. Bertagnolli, "Example of a negative effective Poisson's ratio," Physical Review Letters **47**, 712 (1981).

[36] K. E. Evans, M. A. Nkansah, I. J. Hutchinson, and S. C. Rogers, "Molecular network design," Nature **353**, 124–124 (1991).

[37] K. E. Evans, A. Alderson, and F. R. Christian, "Auxetic two-dimensional polymer networks. an example of tailoring geometry for specific mechanical properties," Journal of the chemical society, Faraday transactions **91**, 2671–2680 (1995).

[38] J. N. Grima, R. Jackson, A. Alderson, and K. E. Evans, "Do zeolites have negative Poisson's ratios?" Advanced Materials **12**, 1912–1918 (2000).

[39] N. Pour, L. Itzhaki, B. Hoz, E. Altus, H. Basch, and S. Hoz, "Auxetics at the molecular level: a negative Poisson's ratio in molecular rods," Angewandte Chemie International Edition **45**, 5981–5983 (2006).

[40] J.-W. Jiang, S. Y. Kim, and H. S. Park, "Auxetic nanomaterials: Recent progress and future development," Applied Physics Reviews **3**, 041101 (2016).

[41] C. Huang and L. Chen, "Negative Poisson's ratio in modern functional materials," Advanced Materials **28**, 8079–8096 (2016).

[42] A. Yeganeh-Haeri, D. J. Weidner, and J. B. Parise, "Elasticity of α-cristobalite: a silicon dioxide with a negative poisson's ratio," Science **257**, 650–652 (1992).

[43] K. L. Alderson, A. P. Pickles, P. J. Neale, and K. E. Evans, "Auxetic polyethylene: the effect of a negative Poisson's ratio on hardness," Acta Metallurgica et Materialia **42**, 2261–2266 (1994).

[44] R. Lakes, "Foam structures with a negative Poisson's ratio," Science **235**, 1038–1041 (1987).

[45] N. R. Keskar and J. R. Chelikowsky, "Negative Poisson ratios in crystalline SiO_2 from first-principles calculations," Nature **358**, 222–224 (1992).

[46] R. H. Baughman, J. M. Shacklette, A. A. Zakhidov, and S. Stafström, "Negative Poisson's ratios

as a common feature of cubic metals," Nature **392**, 362–365 (1998).

[47]l. j. Hall, v. r. coluci, d. s. galvão, m. e. kozlov, m. zhang, s. o. dantas, and r. h. baughman, "Sign change of Poisson's ratio for carbon nanotube sheets," Science **320**, 504–507 (2008).

[48]P. Mardling, A. Alderson, N. Jordan-Mahy, and C. L. Le Maitre, "The use of auxetic materials in tissue engineering," Biomaterials science **8**, 2074–2083 (2020).

[49]Y. J. Park and J. K. Kim, "The effect of negative Poisson's ratio polyurethane scaffolds for articular cartilage tissue engineering applications," Advances in Materials Science and Engineering **2013** (2013).

[50]K. E. Evans and A. Alderson, "Auxetic materials: functional materials and structures from lateral thinking!" Advanced materials **12**, 617–628 (2000).

[51]L. Rothenburg, A. I. A. I. Berlin, and R. J. Bathurst, "Microstructure of isotropic materials with negative Poisson's ratio," Nature **354**, 470–472 (1991).

[52]L. J. Gibson and M. F. Ashby, "Frontmatter," in *Cellular Solids: Structure and Properties*, Cambridge Solid State Science Series (Cambridge University Press, 1997) pp. i–vi, 2nd ed.

[53]F. Milstein and K. Huang, "Existence of a negative Poisson ratio in fcc crystals," Physical Review B **19**, 2030 (1979).

[54]G. Qin and Z. Qin, "Negative Poisson's ratio in two-dimensional honeycomb structures," npj Computational Materials **6**, 1–6 (2020).

[55]J.-W. Jiang and H. S. Park, "Negative poisson's ratio in single-layer black phosphorus," Nature communications **5**, 1–7 (2014).

[56]J.-W. Jiang, T. Chang, X. Guo, and H. S. Park, "Intrinsic negative Poisson's ratio for single-layer graphene," Nano letters **16**, 5286–5290 (2016).

[57]C. He, P. Liu, and A. C. Griffin, "Toward negative Poisson ratio polymers through molecular design," Macromolecules **31**, 3145–3147 (1998).

[58]R. H. Baughman and D. S. Galvao, "Crystalline networks with unusual predicted mechanical and thermal properties," Nature **365**, 735–737 (1993).

[59]E. Jin, I. S. Lee, D. Kim, H. Lee, W.-D. Jang, M. S. Lah, S. K. Min, and W. Choe, "Metal-organic framework based on hinged cube tessellation as transformable mechanical metamaterial," Science advances **5**, eaav4119 (2019).

[60]M. R. Ryder, B. Civalleri, G. Cinque, and J.-C. Tan, "Discovering connections between terahertz vibrations and elasticity underpinning the collective dynamics of the HKUST-1 metal–organic framework," CrystEngComm **18**, 4303–4312 (2016).

[61] A. Mattoni, A. Filippetti, M. I. Saba, and P. Delugas, "Methylammonium rotational dynamics in lead halide perovskite by classical molecular dynamics: the role of temperature," The Journal of Physical Chemistry C **119**, 17421–17428 (2015).

[62] S. Plimpton, "Fast parallel algorithms for short-range molecular dynamics," Journal of computational physics **117**, 1–19 (1995).

[63] W. G. Hoover, "Canonical dynamics: Equilibrium phase-space distributions," Physical review A **31**, 1695 (1985).

[64] A. P. Thompson, S. J. Plimpton, and W. Mattson, "General formulation of pressure and stress tensor for arbitrary many-body interaction potentials under periodic boundary conditions," The Journal of chemical physics **131**, 154107 (2009).

[65] D. Surblys, H. Matsubara, G. Kikugawa, and T. Ohara, "Application of atomic stress to compute heat flux via molecular dynamics for systems with many-body interactions," Physical Review E **99**, 051301 (2019).

[66] P. Boone, H. Babaei, and C. E. Wilmer, "Heat flux for many-body interactions: corrections to lammps," Journal of chemical theory and computation **15**, 5579–5587 (2019).

[67] K. R. Hahn, M. Puligheddu, and L. Colombo, "Thermal boundary resistance at si/ge interfaces determined by approach-to-equilibrium molecular dynamics simulations," Physical Review B **91**, 195313 (2015).

[68] J. Feng, "Mechanical properties of hybrid organic-inorganic $CH_3NH_3BX_3$ (B= Sn, Pb; X= Br, I) perovskites for solar cell absorbers," Apl Materials **2**, 081801 (2014).

[69] F. Shimizu, S. Ogata, and J. Li, "Theory of shear banding in metallic glasses and molecular dynamics calculations," Materials transactions , 2923–2927 (2007).

[70] D. G. Cahill, S. K. Watson, and R. O. Pohl, "Lower limit to the thermal conductivity of disordered crystals," Physical Review B **46**, 6131 (1992).

[71] P. B. Allen and J. L. Feldman, "Thermal conductivity of glasses: Theory and application to amorphous Si," Physical review letters **62**, 645 (1989).

[72] H. Ma, Y. Ma, H. Wang, C. Slebodnick, A. Alatas, J. J. Urban, and Z. Tian, "Experimental Phonon Dispersion and Lifetimes of Tetragonal $CH_3NH_3PbI_3$ Perovskite Crystals," The Journal of Physical Chemistry Letters **10**, 1–6 (2019), https://doi.org/10.1021/acs.jpclett.8b03419.

[73] N. Li, J. Ren, L. Wang, G. Zhang, P. Hänggi, and B. Li, "Colloquium: Phononics: Manipulating heat flow with electronic analogs and beyond," Rev. Mod. Phys. **84**, 1045–1066 (2012).

[74] K. D. Parrish, A. Jain, J. M. Larkin, W. A. Saidi, and A. J. H. McGaughey, "Origins of thermal

conductivity changes in strained crystals," Physical Review B **90**, 235201 (2014).

[75]A. Giri, J. L. Braun, and P. E. Hopkins, "Reduced dependence of thermal conductivity on temperature and pressure of multi-atom component crystalline solid solutions," Journal of Applied Physics **123**, 015106 (2018).

[76]Z. Cheng, M. Han, P. Yuan, S. Xu, B. A. Cola, and X. Wang, "Strongly anisotropic thermal and electrical conductivities of a self-assembled silver nanowire network," Rsc Advances **6**, 90674–90681 (2016).

[77]A. L. Goodwin, D. A. Keen, and M. G. Tucker, "Large negative linear compressibility of $Ag_3[Co(CN)_6]$," Proceedings of the National Academy of Sciences **105**, 18708–18713 (2008), https://www.pnas.org/content/105/48/18708.full.pdf.

[78]W. Li, M. R. Probert, M. Kosa, T. D. Bennett, A. Thirumurugan, R. P. Burwood, M. Parinello, J. A. K. Howard, and A. K. Cheetham, "Negative linear compressibility of a metal–organic framework," Journal of the American Chemical Society **134**, 11940–11943 (2012).